

# Enhanced thermoelectric performance by lone-pair electrons and bond anharmonicity in the two-dimensional $\text{Ge}_2\text{Y}_2$ family of materials with $Y = \text{N, P, As, or Sb}$

Ao Lou , Qing-Bo Liu, and Hua-Hua Fu <sup>\*</sup>*School of Physics and Wuhan National High Magnetic Field Center, Huazhong University of Science and Technology, Wuhan 430074, People's Republic of China* (Received 3 November 2021; revised 21 January 2022; accepted 9 February 2022; published 25 February 2022)

Using density functional theory combined with the Boltzmann transport equation, the charge, thermal transport, and thermoelectric properties in two-dimensional (2D)  $\text{Ge}_2\text{Y}_2$  ( $Y = \text{N, P, As, or Sb}$ ) monolayers characterized by two structural phases, i.e.,  $\alpha\text{-Ge}_2\text{Y}_2$  and  $\beta\text{-Ge}_2\text{Y}_2$ , have been studied systematically. Our theoretical results demonstrate that the lone-pair electrons have remarkable influences on their lattice thermal conductivity. By performing comparative studies on the two different structures of  $\text{Ge}_2\text{Sb}_2$ , we uncover that the above influences not only originate from the interactions between the lone-pair electrons around Sb atoms and the bonding electrons of the adjacent Ge atom, but also from the interlayer Coulomb repulsive forces of lone-pair electrons distributed in different layers. The latter leads to a strong anharmonicity, which greatly suppresses the lattice thermal conductivity. Thus,  $\alpha\text{-Ge}_2\text{Sb}_2$  monolayer has an ultralow thermal conductivity with 0.19 W/mK, while  $\beta\text{-Ge}_2\text{Sb}_2$  monolayer with 5.1 W/mK at the temperature 300 K. Owing to the ultralow lattice thermal conductivity induced by lone-pair electrons, the predicted maximum value of the thermoelectric figure of merit ( $ZT$ ) reaches 1.2 for  $p$ -type and 1.18 for  $n$ -type doping  $\alpha\text{-Ge}_2\text{Sb}_2$ . Our theoretical results put forward another effective mechanism to design and optimize 2D thermoelectric materials with high thermoelectric conversion efficiency.

DOI: [10.1103/PhysRevB.105.075431](https://doi.org/10.1103/PhysRevB.105.075431)

## I. INTRODUCTION

Thermoelectric technology, enabling a direct conversion from thermal energy to electricity, provides us an alternative way for power generation and refrigeration [1,2]. Due to particular advantages, such as environmental protection and low-cost device preparations, thermoelectric conversion energy possesses great potential to be applied in outer space, industrial waste heat utilization, and other special fields [3–5]. However, low conversion efficiency in thermoelectric materials is still one of the key factors to restrict the widely realistic applications of this energy. It has been recognized that thermoelectric conversion efficiency depends not only on the working environments, but also on the intrinsic properties of thermoelectric materials. Usually, it is characterized by a dimensionless figure of merit  $ZT = S^2\sigma T/(k_l + k_e)$ , to reflect the thermoelectric performance of a given material sample, where  $S$  is Seebeck coefficient,  $\sigma$  is electrical conductivity,  $T$  is ambient temperature, and  $k_l$  and  $k_e$  are lattice and electron thermal conductivity, respectively. Due to the fact that  $S$ ,  $\sigma$ , and  $k_e$  are mutually coupled with each other, it is very difficult to regulate a single parameter to enhance the  $ZT$  value. To deal with this issue, two strategies are usually suggested: one is to apply electronic band engineering to improve electronic properties through enhancing energy band convergence [6–8], and the other is to reduce the lattice thermal conductivity in a realistic material, such as by introducing defect structures or all-scale hierarchical architectures [9,10].

Since graphene was stripped successfully in experiments, many of the two-dimensional (2D) materials, exhibiting exotic properties such as high electric conductivity, have been discovered [11–13]. Some of them have a lattice thermal conductivity much lower than that in bulk materials due to boundary effect, quantum confinement effect, and others. In particular, some 2D materials, such as monolayer transition metal sulfide [14,15], molybdenum carbides [16], and group-III monochalcogenide nanosheets [17,18], have been confirmed experimentally to exhibit excellent thermoelectric performance. For example, the SnSe monolayer hosts both low thermal conductivity and outstanding electronic transport properties, allowing it to exhibit an outstanding  $ZT$  value ( $\approx 2.76$ ), even at high temperatures up to 700 K [19]. These exciting findings indicate that the explorations of new classes of 2D materials are helpful to search for new physical mechanisms to enhance the thermoelectric figure of merit. Recently, several group-IV-V monolayer materials characterized by a single-layer  $X_2Y_2$ -type structure have attracted extensive attention from researchers [20–25], owing to their novel electronic properties. For example, Barreteau *et al.* have successfully built layered SiP, SiAs, GeP, and GeAs, which have a monoclinic crystal structure with the  $C2/m$  space group [26]. The dynamical stability of the monolayer  $\alpha$ - and  $\beta$ - $X_2Y_2$ -family materials were confirmed theoretically [27,28]. Moreover, the experimental synthesis of monolayer SnSb characterized by a honeycomb-lattice structure and the monolayer GeAs nanosheets were also reported recently [29,30]. More interestingly, a large amount of lone-pair electrons also exist in these 2D  $X_2Y_2$ -family materials. These particular properties support that we can apply this class of 2D materials

<sup>\*</sup>hhfu@hust.edu.cn

as an ideal material plateau to explore new mechanisms to enhance and optimize the thermoelectric figure of merit of low-dimensional material systems [31].

It has already been recognized that the electrostatic repulsion between the lone-pair electron and the neighboring bonding electron in three-dimensional (3D) bulk materials displays an obvious influence on their lattice thermal conductivity. For example, the lone-pair electrons in the semiconductor  $\text{Cu}_3\text{SbSe}_3$  contribute to form anharmonic Sb-Se bonds, resulting in an ultralow lattice thermal conductivity [32], and a similar feature was found in other 3D materials, such as  $\text{AgSbSe}_2$  [33],  $\text{CuSbSe}_2$  [34], and  $\text{BiSbS}_3$  [35]. The influences of lone-pair electrons on the lattice thermal conductivity in low-dimensional materials, however, are not yet fully understood. In particular, in some previous works, the lone-pair electrons are reported not to play a similar role on thermoelectric performance as that in the 3D bulk materials mentioned above. For example, the lone-pair electrons in the 2D Penta-CN<sub>2</sub> monolayer cannot obviously reduce the lattice thermal conductivity to enhance its thermoelectric conversion efficiency [36]. Therefore, to study the influences of lone-pair electrons on the thermoelectric performance in 2D materials, two questions naturally arise: (i) how to exhibit the lone-pair electrons playing the positive roles on the enhancement of the thermoelectric figure of merit by using band engineering or other effective ways, and (ii) how to understand the influence of bond anharmonicity on the thermoelectric performance in a realistic 2D material.

In order to clearly demonstrate the above two issues, in this paper, we investigate symmetrically the thermoelectric properties of 2D  $\text{Ge}_2\text{Y}_2$  monolayers ( $Y = \text{N}, \text{P}, \text{As}, \text{or Sb}$ ) which possess a large amount of controllable lone-pair electrons, by using first-principles calculations combined with the Boltzmann transport theory. Firstly, the first-principles calculations show that the all  $\text{Ge}_2\text{Y}_2$  monolayers have excellent dynamical stability and are characterized by two stable structural phases, i.e.,  $\alpha\text{-Ge}_2\text{Y}_2$  and  $\beta\text{-Ge}_2\text{Y}_2$ , and all of them display semiconducting properties. Secondly, the lattice thermal conductivity of  $\alpha\text{-Ge}_2\text{Y}_2$  is always smaller with an order of magnitude than that of  $\beta\text{-Ge}_2\text{Y}_2$  with the same components, which helps us to uncover another physical mechanism to enhance the thermoelectric performance in 2D materials. Thirdly, our calculations demonstrate that the spatial distributions of lone-pair electrons in  $\text{Ge}_2\text{Y}_2$  largely influence their lattice thermal conductivity, since the spatial symmetries of lone-pair electrons in  $\alpha$ - and  $\beta\text{-Ge}_2\text{Y}_2$  monolayers are much different. More interestingly, the lone-pair electrons in  $\alpha\text{-Ge}_2\text{Sb}_2$  lead to weaker Ge-Ge bonds while stronger anharmonicity, in comparison with the corresponding parameters in  $\beta\text{-Ge}_2\text{Sb}_2$ . As a result, a rather lower thermal conductivity occurs in  $\alpha\text{-Ge}_2\text{Sb}_2$  with 0.19 W/mK (while 5.1 W/mK in  $\beta\text{-Ge}_2\text{Sb}_2$ ) at 300 K. Owing to the ultralow lattice thermal conductivity, the maximum value of  $ZT$  in  $\alpha\text{-Ge}_2\text{Sb}_2$  reaches 1.2 for  $p$ -type doping and 1.18 for the  $n$ -type doping example at 300 K, while in  $\beta\text{-Ge}_2\text{Sb}_2$ , 1.08 for the  $n$ -type doping at 500 K. Our theoretical results not only uncover that a new class of 2D materials (i.e., the  $\alpha\text{-Ge}_2\text{Sb}_2$  monolayers) can be worked as high-performance and room-temperature thermoelectric materials, but also clarify how to improve the thermoelectric performance of 2D materials by using lone-pair electrons and bond anharmonicity.

The remainder of this paper is organized as follows. In Sec. II, the theoretical methods to calculate the electronic and phononic structures, the lattice thermal conductivity, the Grüneisen dispersions, the carriers' transport properties, the Seebeck coefficients, and the thermoelectric figure of merit are introduced. In Sec. III, the numerical results, including crystal structural and bonding properties, phonon and thermal conductivity properties, and thermoelectric performances in the  $\alpha$ - and  $\beta\text{-Ge}_2\text{Sb}_2$  monolayers are discussed in detail, and the influences of the spatial distributions of lone-pair electrons on the thermoelectric conversion efficiency are also demonstrated. The main results are summarized in the final section, Sec. IV.

## II. THEORETICAL METHODS

### A. Density functional theory calculations

The crystal structures of all  $\text{Ge}_2\text{Y}_2$  monolayers are optimized by utilizing the density functional theory (DFT) based on the projector augmented wave method, as implemented in the Vienna *ab initio* simulation package (VASP) [37,38]. To perform the first-principles calculations, the generalized gradient approximation of Perdew-Burke-Ernzerhof is chosen for the exchange correlation potential [39,40]. To avoid inter-layer interactions, a 15 Å vacuum layer is added between two nearest monolayers in the out-of-plane direction. The cutoff energy for the plane-wave expansion is set as 700 eV, and a Monkhorst-Pack  $k$  mesh [41] of  $15 \times 15 \times 1$  is adopted in the first Brillouin zone (BZ). Both atomic positions and lattice constants in all structures are optimized fully. To obtain well satisfied results, the convergence criterions of energy and force are set as  $10^{-8}$  eV and  $0.001$  eV/Å, respectively.

The electronic band structures of  $\text{Ge}_2\text{Y}_2$  monolayers are calculated by using the linearized augmented plane wave method [42,43] within the WIEN-2K program code [44]. The convergence of matrix size is set as  $R_{\text{MT}} \times K_{\text{MAX}} = 8.5$ , where  $R_{\text{MT}}$  is the smallest one of all atomic sphere radii and  $K_{\text{MAX}}$  is the plane-wave cutoff. For self-consistent calculations, a dense Brillouin sampling of  $47 \times 47 \times 8$  is used and the total energy is converged to  $10^{-4}$  Ry. To avoid the underestimation of the band gap by using the generalized gradient approximation, more accurate band gaps are calculated by performing Tran-Blaha modified Becke-Johnson functions [45]. Because of heavy atoms existing in the all structures, the spin-orbit coupling (SOC) is considered throughout.

It is noted that to confirm the dynamic stability of all  $\text{Ge}_2\text{Y}_2$  monolayers, their phonon spectra are calculated by using the PHONOPY package [46] with a finite-displacement step of 0.01 Å. A supercell containing 100 atoms is adopted for all crystal structures and the Brillouin sampling is set to be  $5 \times 5 \times 1$ . There are eight symmetry-reduced displacements considered for the  $\alpha$ -type configuration, while four symmetry-reduced displacements are considered for the  $\beta$ -type configuration.

### B. Lattice thermal conductivity

The lattice thermal properties of all  $\text{Ge}_2\text{Y}_2$  monolayers are simulated by solving the linear Boltzmann transport equation (BTE) iteratively considering a three-phonon scattering

process [47,48]. The lattice thermal conductivity  $k_{\text{latt}}$  can be expressed by the sum of contributions over all the phonon modes  $\lambda$  as

$$k_{\text{latt}} = \frac{1}{NV\kappa_B T^2} \sum_{\lambda} (\hbar\omega_{\lambda})^2 f_0(f_0 + 1) v_{\lambda}^{\alpha} v_{\lambda}^{\beta}, \quad (1)$$

where  $N$  is the number of wave vectors included in the first BZ,  $V$  is the volume of the crystallographic unit cell,  $\omega_{\lambda}$  is the angular frequency corresponding to a phonon mode  $\lambda$ ,  $f_0$  is the equilibrium Bose-Einstein distribution function, and  $v_{\lambda}$  is the phonon group velocity which is determined by  $v_{\lambda} = \frac{1}{\hbar} \frac{\partial \varepsilon_{i,k}}{\partial k_{\lambda}}$ . The linearized BTE of  $F_{\lambda}^{\beta}$  can be written as  $F_{\lambda} = \tau_{\lambda}^0 (v_{\lambda} + \Delta_{\lambda})$ , in which  $\tau_{\lambda}^0$  denotes the relaxation time which can be obtained by the three-phonon transition probabilities  $\sum_{\lambda'\lambda''}^{\pm} \Gamma_{\lambda'\lambda''}^{\pm}$  summed with the corresponding isotopic disorder term  $\sum_{\lambda'}^{-} \Gamma_{\lambda'\lambda''}$  described in the followings:

$$\frac{1}{\tau_{\lambda}^0} = \frac{1}{N} \left\{ \sum_{\lambda'\lambda''}^{+} \Gamma_{\lambda'\lambda''}^{+} + \sum_{\lambda'\lambda''}^{-} \frac{1}{2} \Gamma_{\lambda'\lambda''}^{-} + \sum_{\lambda'}^{-} \Gamma_{\lambda'\lambda''} \right\}, \quad (2)$$

$$\Gamma_{\lambda'\lambda''}^S = \frac{\hbar\pi\varphi_1\varphi_2}{4\omega_{\lambda}\omega_{\lambda'}\omega_{\lambda''}} |V_{\lambda'\lambda''\lambda}^{\pm}|^2, \quad (3)$$

$$\sum_{\lambda'} \Gamma_{\lambda\lambda'} = \frac{\pi\omega^2}{2} \sum_i g(i) |e_{\lambda}^*(i) e_{\lambda'}^*(i)|^2 \delta(\omega_{\lambda} - \omega_{\lambda'}). \quad (4)$$

Note that in Eq. (3), the index  $S$  indicates  $+$  or  $-$ , corresponding to the absorption or the emission process. For  $S = +$ ,  $\varphi_1 = (f_0' - f_0'')$  and  $\varphi_2 = \delta(\omega_{\lambda} + \omega_{\lambda'} - \omega_{\lambda''})$ , while for  $S = -$ ,  $\varphi_1 = (f_0' + f_0'' + 1)$  and  $\varphi_2 = \delta(\omega_{\lambda} - \omega_{\lambda'} - \omega_{\lambda''})$ . The scattering matrix elements  $V_{\lambda'\lambda''\lambda}^{\pm}$  are associated with the anharmonic force constants (FCs), which can be obtained from DFT calculations. Moreover, the anharmonic FCs are obtained by using the PHONOPY package [46] with a finite-displacement step of 0.01 Å. To perform the numerical calculations, a  $3 \times 3 \times 1$  supercell and a cutoff radius of 0.6 nm are adopted, and the  $q$ -point mesh is employed  $30 \times 30 \times 1$  to obtain a converged lattice thermal conductivity as implemented in the SHENGBTE package [49].

### C. Electrical transport properties

The electrical transport properties of  $\text{Ge}_2\text{Y}_2$  monolayers are studied by solving the semiclassical BTE, the thermoelectric parameters are calculated by using rigid band approximation, and the related constant scattering times are embedded in the BOLTZTRAP code [50]. In particular, the electrical conductivity ( $\sigma_{\alpha\beta}$ ), the electrical thermal conductivity ( $k_{\alpha\beta}^e$ ), and the Seebeck coefficient ( $S_{\alpha\beta}$ ) can be obtained by the following relations:

$$\sigma_{\alpha\beta}(T, \mu) = \frac{1}{V} \int \sigma_{\alpha\beta}(\varepsilon) \left[ -\frac{\partial f_{\mu}(T, \varepsilon)}{\partial \varepsilon} \right] d\varepsilon, \quad (5)$$

$$k_{\alpha\beta}^e(T, \mu) = \frac{1}{e^2 TV} \int \sigma_{\alpha\beta}(\varepsilon) (\varepsilon - \mu)^2 \left[ -\frac{\partial f_{\mu}(T, \varepsilon)}{\partial \varepsilon} \right] d\varepsilon, \quad (6)$$

$$S_{\alpha\beta}(T, \mu) = \frac{1}{eTV\sigma_{\alpha\beta}} \int \sigma_{\alpha\beta}(\varepsilon - \mu) \left[ -\frac{\partial f_{\mu}(T, \varepsilon)}{\partial \varepsilon} \right] d\varepsilon. \quad (7)$$

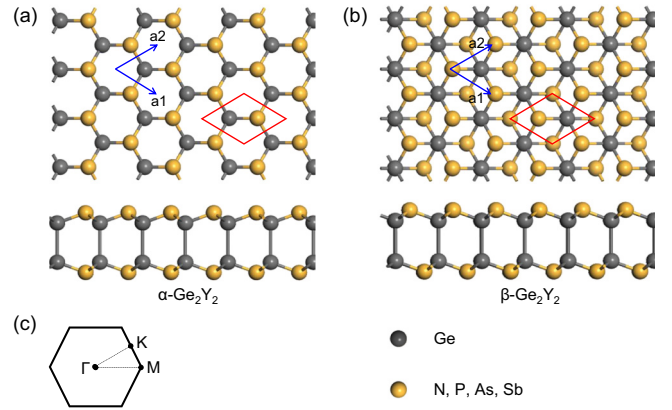


FIG. 1. Top and side views of crystal structures of monolayer  $\alpha\text{-Ge}_2\text{Y}_2$  in (a) and  $\beta\text{-Ge}_2\text{Y}_2$  in (b) ( $Y = \text{N, P, As, or Sb}$ ), respectively. (c) The first Brillouin zone of the above two crystal structures.

In the above three equations,  $\sigma_{\alpha\beta}(\varepsilon)$  is determined by

$$\sigma_{\alpha\beta}(\varepsilon) = \frac{e^2}{N} \sum_{i,k} \tau_{i,k} v_{\alpha}(i, k) v_{\beta}(i, k) \frac{\delta(\varepsilon - \varepsilon_{i,k})}{d\varepsilon}, \quad (8)$$

where  $v$  is the group velocity of the semiclassically treated carriers in a specific band, and  $V$  and  $T$  stand for the unit cell volume and the electron temperature, respectively. The relaxation time  $\tau$  is estimated by deformation potential theory at two dimensions [51]:

$$\tau = \frac{\hbar^3 C_{2D}}{k_B T m^* E_l^2}, \quad (9)$$

where the parameters  $C_{2D}$ ,  $m^*$ , and  $E_l$  are the modulus of elasticity, the mean effective mass, and the deformation potential constant, respectively.

## III. RESULTS AND DISCUSSION

### A. Crystal structures and bonding properties

As drawn in Fig. 1, the all structures of  $\text{Ge}_2\text{Y}_2$  ( $Y = \text{N, P, As, or Sb}$ ) monolayers are illustrated by replacing atoms and after sufficient structural relaxation. One can see that the material examples are composed of two Ge-Y monolayers connected by Ge-Ge bonds, and constructed by two stablest phases with hexagonal structures, which belong to two different point groups, i.e.,  $D_{3h}$  for  $\alpha\text{-Ge}_2\text{Y}_2$  while  $D_{3d}$  for  $\beta\text{-Ge}_2\text{Y}_2$  monolayer, as drawn in Figs. 1(a) and 1(b), respectively. For example, the detailed lattice parameters of two different structures of  $\text{Ge}_2\text{Sb}_2$  monolayer are listed in Table I, and the structural parameters of other material samples are provided in Supplemental Material Table S1 [52]. Our first-principles calculations show that the lattice parameters of  $\alpha\text{-Ge}_2\text{Y}_2$  are well consistent with some previous reports [24,28]. However, our calculations demonstrate that the lattice constants of  $\alpha\text{-Ge}_2\text{Y}_2$  have slight differences from those of  $\beta\text{-Ge}_2\text{Y}_2$ , which is different from the results reported in some previous works [27]. The main reason is that the lone-pair electrons are considered fully in the all structures studied here. Otherwise, the numerical results for these two structures of  $\text{Ge}_2\text{Y}_2$  are in good agreement with the previous ones [24,28]. Moreover, the

optimized lattice and thickness constants for  $\alpha$ - $\text{Ge}_2\text{Sb}_2$  are 4.123 and 5.014 Å, while for  $\beta$ - $\text{Ge}_2\text{Sb}_2$  they are 4.133 and 4.983 Å, respectively. In particular, the Ge-Ge bond length in  $\alpha$ - $\text{Ge}_2\text{Sb}_2$  (2.499 Å) is longer than the corresponding bond in  $\beta$ - $\text{Ge}_2\text{Sb}_2$  (2.481 Å), indicating that the Ge-Ge bond in  $\alpha$ - $\text{Ge}_2\text{Sb}_2$  monolayer is relatively weak.

To understand the bond properties in the two different phases of  $\text{Ge}_2\text{Sb}_2$  monolayers, their electron localization functions (ELFs) [53] are firstly calculated. The ELF can be utilized to quantitatively identify the characters of chemical bonds between the nearest atoms and to examine the electrons' pairing property, helping to determine the spatial distributions of special electrons including lone-pair electrons. Usually, the ELF is defined by  $\text{ELF} = (1 + \{K(r)/K_h[\rho(r)]\}^2)^{-1}$ , where  $K$  is the curvature of electronic pair density for the electrons with identical spin indexes,  $\rho(r)$  is the density at position  $r$ , and  $K_h[\rho(r)]$  is the value of  $K$  in a homogeneous electron gas with density  $\rho$ . It is noted that ELF is a dimensionless localization index restricted to the region from 0 to 1. A high ELF value, such as  $\text{ELF} = 1$ , stands for a low probability of finding a second electron with the same spin in the neighboring region of reference electron. That is to say that the reference electron is highly localized in this case. While for a low ELF value, such as  $\text{ELF} = 0$ , the reference electron is much delocalized.

Figures 2(a) and 2(b) demonstrate the calculated 3D ELFs (isosurface level of 0.9572) for  $\alpha$ - and  $\beta$ - $\text{Ge}_2\text{Sb}_2$  monolayer, respectively. The mushroom shape of electrons around Sb atoms clearly indicates the existence of lone-pair electrons, which are completely localized and tend to distribute upwards or downwards related to the plane. Moreover, the electrons sharing in different structural phases can be better visualized by using a 2D ELF map. As drawn in Figs. 2(c) and 2(d) from the side view, the ELF of lone-pair electrons in Sb atoms is just in the shape of wick. More interestingly, the lone-pair electrons in  $\alpha$ - $\text{Ge}_2\text{Sb}_2$  monolayer are strictly symmetrical about the plane, while in  $\beta$ - $\text{Ge}_2\text{Sb}_2$ , they are nearly antisymmetrical about the plane, indicating that the lone-pair electrons will lead to different properties in these two different configurations, giving us an ideal material platform to study the influences of the lone-pair electrons with opposite spatial symmetries on their thermoelectric performance. From the top view in Figs. 2(e) and 2(f), however, the spatial distributions of lone-pair electrons are similar to each other. According to the valence shell electron pair repulsion theory [54], both Ge-Ge bonding and Ge-Sb bonding are  $sp^3$  hybridized and the Sb atom has five valence electrons in its outermost shell. Thus, the three valence electrons of the Sb atom form bonds with the valence electrons in the Ge atom, while the two remaining electrons in the  $sp^3$  orbital tend to form two independent lone-pair electrons. According to the prediction from

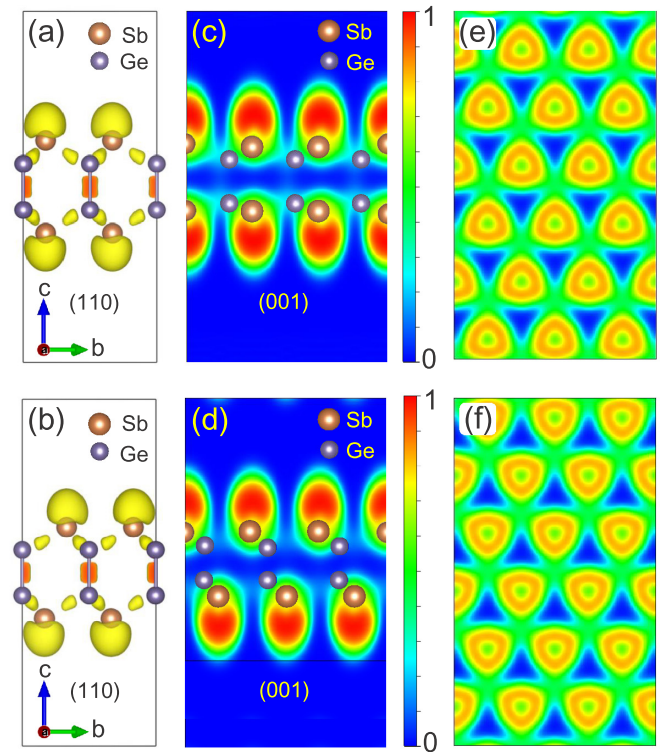


FIG. 2. (a), (c), and (e) The electronic localization function (ELF), and their projections on the (110) and (001) planes for  $\alpha$ - $\text{Ge}_2\text{Sb}_2$ . (b), (d), and (f) The ELF, and their projections on the (110) and (001) planes for  $\beta$ - $\text{Ge}_2\text{Sb}_2$ .

Zhang *et al.* [31,32], as the electronegativity is different, the electronic repulsion between the lone-pair electrons and the nearby bonded electrons may lead to the different bonding angle. As a result, the large asymmetric distortions of lone-pair electrons in  $\alpha$ - $\text{Ge}_2\text{Sb}_2$  provide a large possibility to produce strong anharmonicity, which contributes to reduce the lattice thermal conductivity of material examples.

Going back to the previous two structural phases of  $\text{Ge}_2\text{Sb}_2$  monolayers, although the lone-pair electrons are distributed uniformly in the plane and characterized by the same tendency out of plane, the bonding angles in them are still different. The Sb-Ge-Sb bonding angle in  $\alpha$ - $\text{Ge}_2\text{Sb}_2$  is  $99.941^\circ$ , less than the corresponding angle of  $100.167^\circ$  in  $\beta$ - $\text{Ge}_2\text{Sb}_2$ . What leads to this difference? To answer this question, we should take into account the Coulomb repulsion between two nearest lone-pair electrons localized in different layers. As illustrated in Table I, the atomic distance between the top Sb and the bottom Sb atoms in a unit cell is 5.014 Å in  $\alpha$ - $\text{Ge}_2\text{Sb}_2$  and 5.525 Å in  $\beta$ - $\text{Ge}_2\text{Sb}_2$ , and the distances between the nearest lone-pair electrons in both structures have similar values.

TABLE I. The crystal structure parameters of  $\alpha$ - and  $\beta$ - $\text{Ge}_2\text{Sb}_2$  monolayers (in units of Å).

|                                     | Lattice constants<br>$a = b$ | Bond length<br>Ge-Ge | Bond length<br>Ge-Sb | Thickness<br>$\sigma$ | Atomic distance<br>Sb-Sb (out-of-plane) |
|-------------------------------------|------------------------------|----------------------|----------------------|-----------------------|---|
| $\alpha$ - $\text{Ge}_2\text{Sb}_2$ | 4.123                        | 2.499                | 2.692                | 5.014                 | 5.014                                   |
| $\beta$ - $\text{Ge}_2\text{Sb}_2$  | 4.133                        | 2.481                | 2.694                | 4.983                 | 5.529                                   |

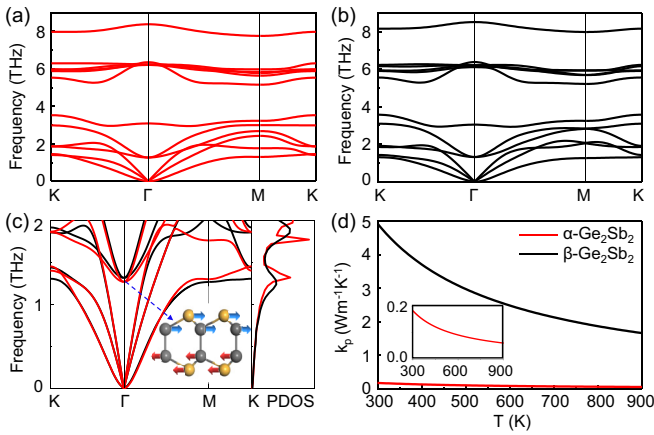


FIG. 3. Phonon dispersions of (a)  $\alpha$ - $\text{Ge}_2\text{Sb}_2$  monolayer and (b)  $\beta$ - $\text{Ge}_2\text{Sb}_2$  monolayer. (c) The comparison of phonon spectra and the PDOS of two structures at low frequencies; the red and black lines denote  $\alpha$ - $\text{Ge}_2\text{Sb}_2$  and  $\beta$ - $\text{Ge}_2\text{Sb}_2$ , respectively. The inset denotes the lattice vibration mode of the lowest frequency optical band in the  $\alpha$ - $\text{Ge}_2\text{Sb}_2$  monolayer. (d) The lattice thermal conductivity for two structures as a function of temperature; the inset is the magnification of thermal conductivity in  $\alpha$ - $\text{Ge}_2\text{Sb}_2$ , showing the inversely proportional temperature property of lattice thermal conductivity.

Moreover, the shorter distance between two nearest lone-pair electrons indicates the stronger electronic repulsion. Therefore,  $\alpha$ - $\text{Ge}_2\text{Sb}_2$  has less lattice constants, longer Ge-Ge bond length, and smaller angle of Sb-Ge-Sb. It is noted that the ELF value of the region between Ge-Ge in  $\alpha$ - $\text{Ge}_2\text{Sb}_2$  monolayer is approximate to 0.8783, smaller than the corresponding ELF value of 0.9042 in  $\beta$ - $\text{Ge}_2\text{Sb}_2$  monolayer, suggesting a weak Ge-Ge bond in the former, while a stronger Ge-Ge bond in the latter, confirming further the above conclusion. Furthermore, owing to the fact that the  $\alpha$ - $\text{Ge}_2\text{Sb}_2$  monolayer has stronger repulsion between two neighboring lone-pair electrons than that in  $\beta$ - $\text{Ge}_2\text{Sb}_2$  monolayer, a stronger anharmonicity may be induced in the former, which helps to enhance the phonon scattering and to reduce the lattice thermal conductivity.

### B. Phonon and thermal conductivity properties

The calculated phonon dispersions of  $\alpha$ - and  $\beta$ - $\text{Ge}_2\text{Sb}_2$  monolayers are illustrated in Figs. 3(a) and 3(b), respectively, and the phonon dispersions of  $\text{Ge}_2\text{N}_2$ ,  $\text{Ge}_2\text{P}_2$ , and  $\text{Ge}_2\text{As}_2$  monolayers are provided in Supplemental Material, Fig. S1 [52]. One can find that there are not any imaginary parts of phonon frequencies in the first BZ for all material samples, indicating that their structures are dynamically stable. Moreover, both  $\alpha$ - and  $\beta$ - $\text{Ge}_2\text{Sb}_2$  monolayers display approximately identical dispersions, owing to their same atomic masses. We well know that the lattice thermal conductivity is mainly determined by the dispersion relations at low frequencies, thus it is necessary to perform comparative studies on the phonon spectra of both structures. As described in Fig. 3(c), near the high-symmetry point  $\Gamma$ , their acoustic branches show the same dispersion relationship, while near the high-symmetry points  $M$  and  $K$ ,  $\beta$ - $\text{Ge}_2\text{Sb}_2$  has lower frequencies in comparison with  $\alpha$ - $\text{Ge}_2\text{Sb}_2$ . In particular, near the high-symmetry point  $\Gamma$ , the atoms tend to vibrate as

a whole as demonstrated in Fig. 3(c). As a result, both phases of  $\text{Ge}_2\text{Sb}_2$  have nearly similar phonon dispersions. However, near the boundary of the BZ (i.e., the points  $M$  and  $K$ ), due to the different structural symmetry of two phases, the atoms tend to vibrate in different modes, leading to the large differences near these points, as illustrated in Fig. 3(c). Moreover, the structural symmetry is tightly associated with the spatial distributions of lone-pair electrons, that is to say, the different symmetries of lone-pair electrons in these two different phases of  $\text{Ge}_2\text{Sb}_2$  also lead to different atomic forces, which determine the properties of mode softening in them. Moreover, the lowest optical branch at point  $\Gamma$  in the  $\alpha$ - $\text{Ge}_2\text{Sb}_2$  monolayer not only displays lower frequencies than the corresponding branch in  $\beta$ - $\text{Ge}_2\text{Sb}_2$ , but also intersects with the acoustic branches. These properties strengthen the couplings among the acoustic-optical branches to produce a sharp phononic density of state (PDOS) peak. In addition, two PDOS peaks appear at the frequency  $f = 1.3$  and  $1.8$  THz in  $\alpha$ - $\text{Ge}_2\text{Sb}_2$  monolayer and are much sharper than the related two peaks in  $\beta$ - $\text{Ge}_2\text{Sb}_2$ , indicating that the lattice thermal conductivity in the former may be largely reduced [55]. It should be noted that the peaks of PDOS are also associated with the asymmetric distributions of lone-pair electrons as discussed above.

To verify the above analysis, we calculated the temperature dependence of lattice thermal conductivity  $k_{\text{latt}}$  in both structures of  $\text{Ge}_2\text{Sb}_2$ , as illustrated in Fig. 3(d), in which the inset denotes the magnification for  $\alpha$ - $\text{Ge}_2\text{Sb}_2$  to highlight the feature of  $T^{-1}$ . Although both structures are isotropic,  $\alpha$ - $\text{Ge}_2\text{Sb}_2$  has much lower  $k_{\text{latt}}$  in comparison with  $\beta$ - $\text{Ge}_2\text{Sb}_2$ . It is interesting that this phenomenon is also found in other examples of  $\text{Ge}_2\text{Y}_2$  (see Supplemental Material, Fig. S2 [52]). In particular, the lattice thermal conductivity of all  $\alpha$ - $\text{Ge}_2\text{Y}_2$  is an order of magnitude smaller than that of the corresponding  $\beta$ - $\text{Ge}_2\text{Y}_2$  possessing the same component and size. As a result, the  $\alpha$ - $\text{Ge}_2\text{Sb}_2$  has an ultralow thermal conductivity with  $0.19 \text{ W m}^{-1} \text{ K}^{-1}$  at room temperature, which is obviously lower than those in other 2D material samples with the structure of double layers [19]. In addition, the  $\beta$ - $\text{Ge}_2\text{Y}_2$  monolayer also displays a low  $k_{\text{latt}}$  value with  $5.25 \text{ W m}^{-1} \text{ K}^{-1}$  at room temperature, which is well consistent with the result in a previous report [56]. The low thermal conductivity obtained here is conducive to design high thermoelectric conversion efficiency, inspiring us to further examine their thermoelectric properties.

Next, we turn to clearly demonstrate the relations between the lone-pair electrons and the ultralow lattice thermal conductivity in these 2D material examples. As described in Fig. 3(c), the lowest optical branch at point  $\Gamma$  is relatively flatter, due to the Ge-Ge coupling between the upper and lower layers. Moreover, the lone-pair electrons repel each other, leading to the different bonding strengths as discussed previously. As a result, the phonon frequencies contributed by lone-pair electrons are also different in both structures. To verify the above conclusion, we turn to examine the charging trends of potential energy of different atoms in both structures. In Figs. 4(a) and 4(b), we describe the potential energy for Sb and Ge atoms as a function of atomic displacement around the equilibrium positions along in-plane and out-of-plane directions in  $\alpha$ - $\text{Ge}_2\text{Sb}_2$  and  $\beta$ - $\text{Ge}_2\text{Sb}_2$ , respectively. Thus, we can

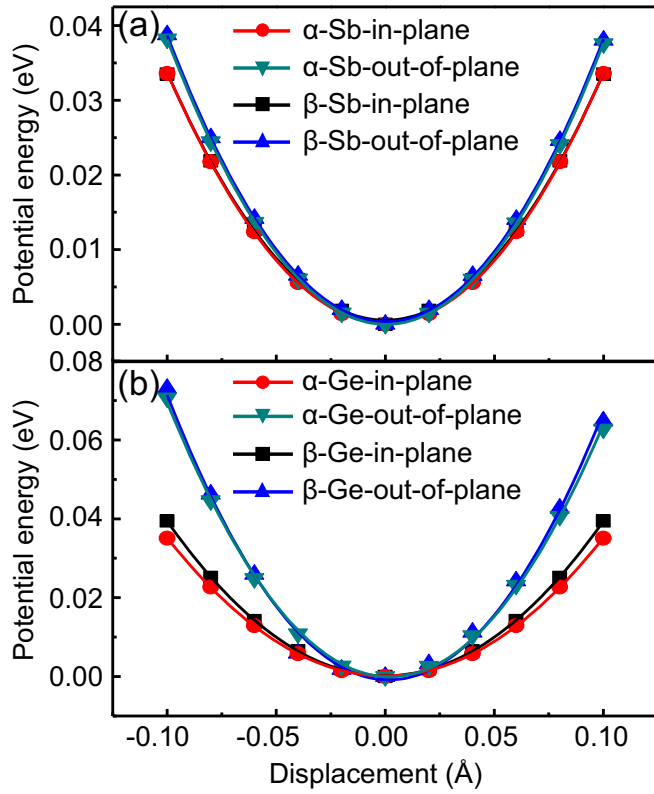


FIG. 4. The calculated potential energy curves for Sb and Ge atoms as a function of displacement around the equilibrium positions along in-plane and out-of-plane directions for  $\alpha$ -Ge<sub>2</sub>Sb<sub>2</sub> and  $\beta$ -Ge<sub>2</sub>Sb<sub>2</sub>.

obtain the basic energy potential required, as the related atom is shifted away from their equilibrium positions in plane and out of plane. For example, the flatter the curve, the less energy is required to move away from their equilibrium positions, indicating the weak restoring forces on the vibrating atoms or the weak bonding [57,58]. From the potential energy surfaces (PESs), we find that the all Sb and Ge atoms are localized in deep potential wells. In particular, for the Sb atom in both structures, the curves of PESs are basically the same. Nevertheless, the PES of Ge atoms in  $\alpha$ -Ge<sub>2</sub>Sb<sub>2</sub> (red line) along in-plane direction are flatter than that in  $\beta$ -Ge<sub>2</sub>Sb<sub>2</sub> (black line) at the same direction [see Fig. 4(b)], indicating that Ge atoms in  $\alpha$ -Ge<sub>2</sub>Sb<sub>2</sub> are looser. Furthermore, the PESs for Ge atoms are almost identical as shown in Fig. 4(b), especially for the small displacements. Such small difference in the PESs is well consistent with the small difference in the Ge-Ge bond lengths ( $\sim 0.03$  Å) and the small difference in bonding angle. Additionally, we find that all the PESs show almost parabolic behavior versus atomic displacement, indicating that the values of lattice distortion will not affect the bond anharmonicity in both structures.

Moreover, the weak Ge-Ge bonds and the loose Ge atoms could strengthen crystal anharmonicity and further scatter phonons, resulting in lower lattice thermal conductivity in  $\alpha$ -Ge<sub>2</sub>Sb<sub>2</sub> monolayer [59,60]. Note that the strength of anharmonicity can be estimated by the Grüneisen parameter [61], which characterizes the relationship between phonon

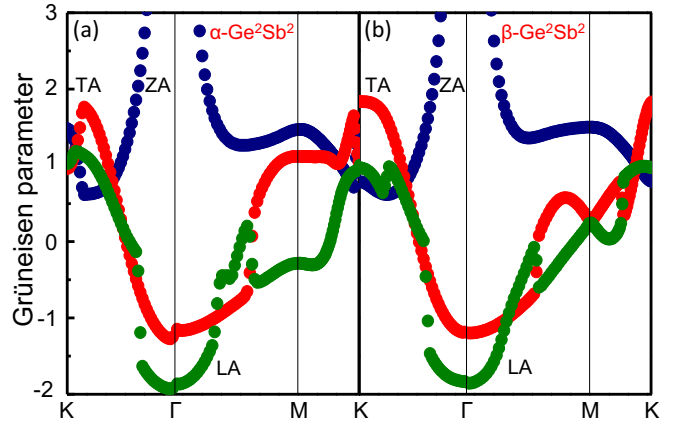


FIG. 5. Calculated Grüneisen dispersions of acoustic branch for (a)  $\alpha$ -Ge<sub>2</sub>Sb<sub>2</sub> and (b)  $\beta$ -Ge<sub>2</sub>Sb<sub>2</sub>. The corresponding TA, ZA, and LA modes are highlighted by red, green, and blue lines, respectively.

frequency and volume change, as defined below:

$$\gamma_i = -\frac{V}{\omega_i} \frac{\partial \omega_i}{\partial V}, \quad (10)$$

where  $V$  is the volume of unit cell and  $\omega_i$  is the frequency of the  $i$ th phonon branch. Figure 5 shows the calculated Grüneisen parameters of flexural acoustic (ZA), transverse acoustic (TA), and longitudinal acoustic (LA) bonds along the high-symmetry paths in the first BZ, respectively. Unlike some other 3D crystal structures, our material examples are isotropic in plane while behaving largely anisotropic out of plane. Consequently, the all lone-pair electrons are arranged in the out-of-plane direction, i.e., perpendicular to the plane. Thus, we cannot directly distinguish the difference of anharmonicity at different directions, especially in the same direction where the lone-pair electrons are mainly located [34]. Nevertheless, we can analyze the in-plane anharmonic induced by lone-pair electrons through comparing with these two different structures. The most important feature drained from Fig. 5 is that in comparison with  $\beta$ -Ge<sub>2</sub>Sb<sub>2</sub>, the unusually high values of Grüneisen parameters in  $\alpha$ -Ge<sub>2</sub>Sb<sub>2</sub> appear along the path  $M$ - $K$ , indicating that along this path, the unusual Grüneisen parameters may be associated with the different lattice thermal conductivities in these two crystal structures of Ge<sub>2</sub>Sb<sub>2</sub>. Moreover, the spatial distributions of lone-pair electrons lead to the different Grüneisen parameters along the path  $M$ - $K$ . It is noted that the mean Grüneisen parameter ( $\bar{\gamma} = \sqrt{\langle \gamma_i^2 \rangle}$ ) for  $\alpha$ -Ge<sub>2</sub>Sb<sub>2</sub> is 2.518, larger than the value of 2.366 for  $\beta$ -Ge<sub>2</sub>Sb<sub>2</sub>. The larger mean Grüneisen parameter indicates strongly anharmonic vibrational properties and low lattice thermal conductivity in the  $\alpha$ -Ge<sub>2</sub>Sb<sub>2</sub> monolayer. In addition, the lone-pair electrons in both structures are distributed uniformly in the plane, thus the interactions between two adjacent lone-pair electrons are the same in them, while an obvious difference still lies in the vertical direction, as demonstrated in Fig. 2. Thus, one can conclude that the different Grüneisen parameters originated from the spatial distributions of lone-pair electrons in 2D allotropes work as the main factor to influence their lattice thermal conductivities.

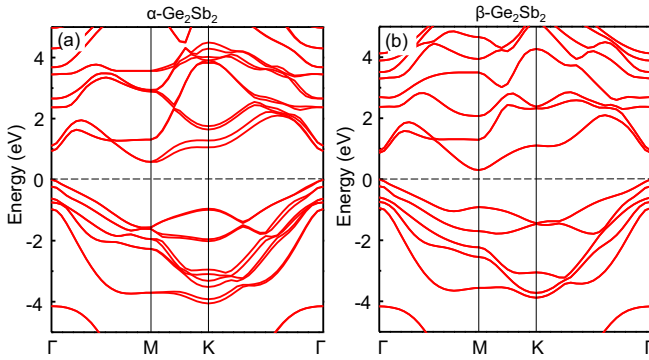


FIG. 6. Electronic band structures of  $\alpha$ - $\text{Ge}_2\text{Sb}_2$  in (a) and  $\beta$ - $\text{Ge}_2\text{Sb}_2$  in (b) along the high-symmetry  $k$  points  $\Gamma$ ,  $M$ ,  $K$ , and  $\Gamma$ .

### C. Thermoelectric properties

Profiting from the low lattice thermal conductivity induced by lone-pair electrons, it is significant to further explore their thermoelectric performance. Firstly, the electronic band structures of  $\alpha$ - and  $\beta$ - $\text{Ge}_2\text{Sb}_2$  monolayers are calculated and drawn in Figs. 6(a) and 6(b), respectively. We find that the band structures of two different phases are similar with each other. In particular, both of them display indirect semiconducting properties, characterized by the conduction band minimum (CBM) and the valence band maximum (VBM) located at points  $M$  and  $\Gamma$ , respectively. These typical properties are also observed in all other  $\text{Ge}_2\text{Y}_2$  monolayers (see Supplemental Material, Fig. S3 [52]). Moreover, the band gap in  $\alpha$ - and  $\beta$ - $\text{Ge}_2\text{Sb}_2$  is 0.58 and 0.31 eV, respectively. This significant difference is originated from SOC. It can be clearly seen that the band splitting occurs in  $\alpha$ - $\text{Ge}_2\text{Sb}_2$ , while the degeneracy of electronic bands appears in  $\beta$ - $\text{Ge}_2\text{Sb}_2$ , indicating that the thermoelectric performance may be enhanced in the latter [62]. However, the CBM valleys localized at the points  $\Gamma$  and  $M$  in  $\alpha$ - $\text{Ge}_2\text{Sb}_2$  tend to be degenerate with a conduction band offset  $\Delta E$  of 0.35 eV [63]. This larger valley degeneracy increases the effective mass  $m^*$  of DOS, leading to a higher Seebeck coefficient  $S$  at the same carrier concentration [6,64]. As a result, the  $n$ -type Seebeck coefficient  $S$  is larger than the  $p$  type for  $\alpha$ - $\text{Ge}_2\text{Sb}_2$ , as well as for  $\beta$ - $\text{Ge}_2\text{Sb}_2$ .

Moreover, the calculated effective masses  $m^*$ , the modulus of elasticity  $C_{2D}$ , and the deformation potential constant  $E_l$  are listed in Table II. Generally, a light-mass band is beneficial to enhance electrical conductivity, while a heavy-mass band is favorable for a good Seebeck coefficient  $S$ . Both for  $\alpha$ - and  $\beta$ - $\text{Ge}_2\text{Sb}_2$  monolayers, the CBM has a larger band effective mass than that of the VBM, which is conducive to

obtain large Seebeck coefficient for  $n$ -type monolayer. This result is consistent with the above one drawn from band degeneracy. For their band structures, we also obtain that the CBM in  $\alpha$ - $\text{Ge}_2\text{Sb}_2$  has a larger band effective mass than the corresponding value in  $\beta$ - $\text{Ge}_2\text{Sb}_2$ . The lower lattice thermal conductivity and the better electronic properties in the  $\alpha$ - $\text{Ge}_2\text{Sb}_2$  monolayer indicate it may exhibit better thermoelectric properties. More than that, the calculated Seebeck coefficients ( $S$ ) and the thermoelectric figure of merit ( $ZT$ ) of both structures verify well the above conclusion. In Figs. 7(a) and 7(b), the thermoelectric coefficient  $S$  is drawn versus the carrier concentration  $n$  at  $T = 300, 500,$  and  $700$  K. We find that  $S$  decreases with increasing  $n$  or with decreasing  $T$  at higher carrier concentrations. Moreover, both for  $\alpha$ - and  $\beta$ - $\text{Ge}_2\text{Sb}_2$  monolayers, the  $n$ -type Seebeck coefficient  $S (> 0)$  is surpassed more largely than the corresponding  $S (< 0)$  in the  $p$  type and meanwhile,  $S$  in  $\beta$ - $\text{Ge}_2\text{Sb}_2$  is surpassed more largely than that in  $\alpha$ - $\text{Ge}_2\text{Sb}_2$  at the same temperature and carrier concentration. In general, a good thermoelectric material should possess a Seebeck coefficient  $S$  larger than  $200 \mu\text{V}/\text{K}$ . Obviously, both structures meet well this criterion. Nevertheless, only a large Seebeck coefficient cannot determine a high thermoelectric figure of merit, which drives us to explore further how to optimize their thermoelectric coefficients.

Figures 7(c) and 7(d) demonstrate the calculated  $ZT$  values of both structures versus the carrier concentration  $n$  at different temperatures. Because the doping generally benefits the electrical conductivity while it suppresses the Seebeck coefficient, the  $ZT$  value firstly increases and then decreases with increasing carrier concentration, helping to optimize the thermoelectric performance. For  $\alpha$ - $\text{Ge}_2\text{Sb}_2$ , the calculated  $ZT$  value of the  $p$  type is slightly larger than the  $n$  type at the optimized carrier concentration and at room temperature, due to the light effective mass of VBM or high electrical conductivity. The optimized  $ZT$  decreases as the temperature increases characterized by the maximum value of  $ZT$  in the  $n$ -type and  $p$ -type  $\alpha$ - $\text{Ge}_2\text{Sb}_2$  is  $1.18 (3.2 \times 10^{19} \text{ electrons}/\text{cm}^3)$  and  $1.2 (1.04 \times 10^{18} \text{ hole}/\text{cm}^3)$  at room temperature, respectively, while for  $\beta$ - $\text{Ge}_2\text{Sb}_2$ , the optimized  $ZT$  value in the  $n$  type is significantly greater than that in the  $p$  type at all temperatures. Due to the higher thermal conductivity in  $\beta$ - $\text{Ge}_2\text{Sb}_2$ , its thermoelectric performance is slightly worse than that in  $\alpha$ - $\text{Ge}_2\text{Sb}_2$ . Different from  $\alpha$ - $\text{Ge}_2\text{Sb}_2$ , the maximum  $ZT$  in the  $n$ -type  $\beta$ - $\text{Ge}_2\text{Sb}_2$  is large to  $1.07 (8.45 \times 10^{19} \text{ electrons}/\text{cm}^3)$  at  $T = 500$  K. Therefore, both structures exhibit excellent thermoelectric properties at all different temperatures, confirming further that the 2D material examples in the IV-V group have potential thermoelectric device applications.

TABLE II. The calculated elasticity modulus ( $C_\beta$ ), deformation potential constants ( $E_l$ ), effective masses ( $m^*$ ), and relaxation time ( $\tau$ ) of holes and electrons in the  $\alpha$ - and  $\beta$ - $\text{Ge}_2\text{Sb}_2$  monolayers, respectively.

|                                     |          | $C_{2D}$ ( $\text{J m}^{-2}$ ) | $E_l$ (eV) | $m^*$ (me) | $\tau$ (s)              |
|-------------------------------------|----------|--------------------------------|------------|------------|-------------------------|
| $\alpha$ - $\text{Ge}_2\text{Sb}_2$ | Hole     | 156.625                        | 2.496      | 0.660      | $4.636 \times 10^{-13}$ |
| $\alpha$ - $\text{Ge}_2\text{Sb}_2$ | Electron | 156.625                        | 3.025      | 2.314      | $9.004 \times 10^{-14}$ |
| $\beta$ - $\text{Ge}_2\text{Sb}_2$  | Hole     | 153.509                        | 0.964      | 0.782      | $1.017 \times 10^{-12}$ |
| $\beta$ - $\text{Ge}_2\text{Sb}_2$  | Electron | 153.509                        | 1.546      | 1.976      | $7.151 \times 10^{-13}$ |

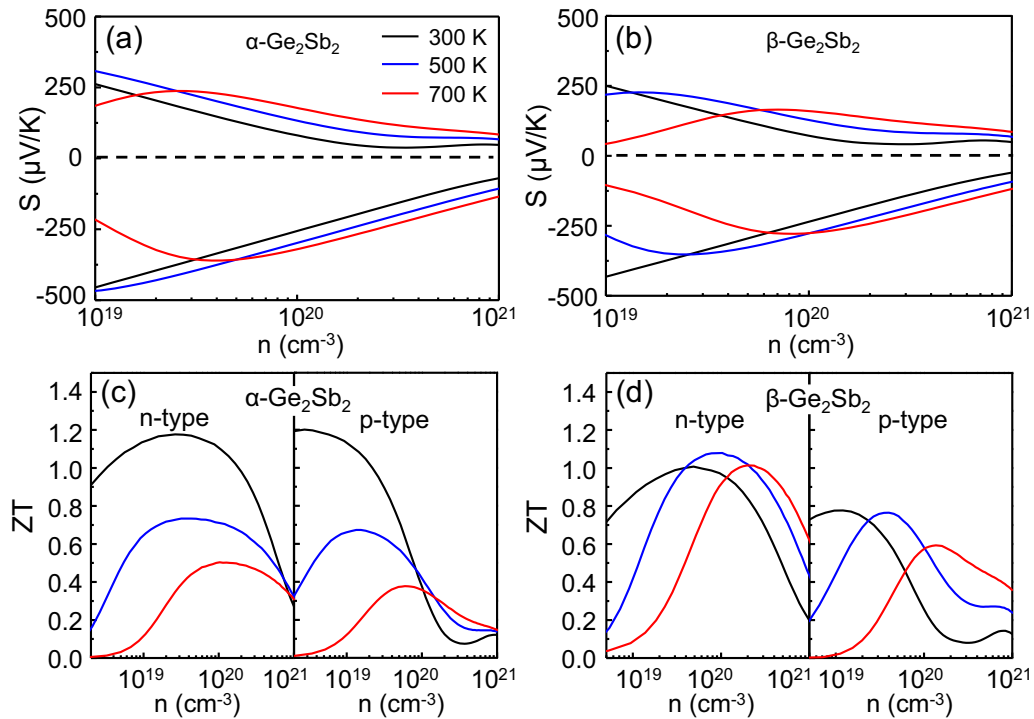


FIG. 7. Calculated Seebeck coefficient ( $S$ ) and thermoelectric figures of merit ( $ZT$ ) as a function of the carrier concentration  $n$  in the different  $\text{Ge}_2\text{Sb}_2$  monolayers. (a) and (c) for the  $n$ -type and  $p$ -type  $\alpha\text{-Ge}_2\text{Sb}_2$  monolayers; (b) and (d) for the  $n$ -type and  $p$ -type  $\beta\text{-Ge}_2\text{Sb}_2$  monolayers.

#### IV. CONCLUSION

In summary, the electronic structures, phononic structures, and thermoelectric properties of the 2D  $\text{Ge}_2\text{Y}_2$ -family materials with two different structural phases have been studied systematically by using density functional theory combined with the Boltzmann transport equation. Through the comparative studies on  $\alpha$ - and  $\beta\text{-Ge}_2\text{Y}_2$  monolayers, we uncover that the lattice thermal conductivities in these two phases are influenced largely by the different phononic dispersions at high-symmetry points, which are originated from the different spatial distributions of lone-pair electrons in different structures. Moreover, due to the different spatial symmetries of lone-pair electrons in the  $\alpha$ - and  $\beta\text{-Ge}_2\text{Y}_2$  monolayers, the Coulomb repulsive forces between the lone-pair electrons in the upper and those in the lower layers are much different, which leads to a stronger bond anharmonicity in the former, while the weaker one in the latter. As a result, the lattice thermal conductivity in the all  $\alpha\text{-Ge}_2\text{Y}_2$  monolayers is nearly

about an order of magnitude smaller than the corresponding one in  $\beta\text{-Ge}_2\text{Y}_2$  possessing the same components. Due to the ultralow lattice thermal conductivity in  $\alpha\text{-Ge}_2\text{Y}_2$  ( $0.19 \text{ W m}^{-1} \text{ K}^{-1}$  at 300 K), the highest  $ZT$  value may reach 1.18 for the  $n$ -type and 1.2 for the  $p$ -type doping at room temperature, while for  $\text{Ge}_2\text{Sb}_2$  ( $5.25 \text{ W m}^{-1} \text{ K}^{-1}$  at 300 K), the highest  $ZT$  value can reach 1.07 for  $n$ -type doping. Our theoretical results not only demonstrate that the lone-pair electrons can be applied as an effective way to enhance the thermoelectric performance in low-dimensional materials, but also uncover that the 2D  $\text{Ge}_2\text{Y}_2$ -family materials in the IV-V group have promising thermoelectric device applications.

#### ACKNOWLEDGMENT

This work is supported by the National Natural Science Foundation of China under Grants No. 11774104, No. U1832209, and No. 12147113.

- [1] Y. Z. Pei, X. Y. Shi, A. LaLonde, H. Wang, L. D. Chen, and G. J. Snyder, Convergence of electronic bands for high performance bulk thermoelectrics, *Nature (London)* **473**, 66 (2011).
- [2] R. J. Mehta, Y. L. Zhang, C. Karthik, B. Singh, R. W. Siegel, T. Borca-Tasciuc, and G. Ramannath, A new class of doped nanobulk high-figure-of-merit thermoelectrics by scalable bottom-up assembly, *Nat. Mater.* **11**, 233 (2012).
- [3] H. J. Goldsmid, *Introduction to Thermoelectricity*, Springer Series in Materials Science (Springer, New York, 2009).

- [4] S. B. Riffat and X.-L. Ma. Thermoelectric: A review of present and potential applications, *Appl. Therm. Eng.* **23**, 913 (2009).
- [5] G. J. Snyder and E. S. Toberer, Complex thermoelectric materials, *Nat. Mater.* **7**, 105 (2008).
- [6] B. Poudel, Q. Hao, Y. Ma, Y.-C. Lan, A. Minnich, B. Yu, X. Yan, D.-Z. Wang, A. Muto, D. Vashaee, X.-Y. Chen, J.-M. Liu, M. S. Dresselhaus, G. Chen, and Z.-F. Ren, High thermoelectric performance of nanostructured bismuth antimony telluride bulk alloys, *Science* **320**, 634 (2008).

- [7] J. P. Heremans, V. Jovovic, E. S. Toberer, A. Saramat, K. Kurosaki, A. Charoenphakdee, S. Yamanaka, and G. J. Snyder, Enhancement of thermoelectric efficiency in PbTe by distortion of the electronic density of states, *Science* **321**, 554 (2008).
- [8] K. Biswas, J.-Q. He, I. D. Blum, C.-L. Wu, T. P. Hogan, D. N. Seidman, V. P. Dravid, and M. G. Kanatzidis, High-performance bulk thermoelectrics with all-scale hierarchical architectures, *Nature (London)* **489**, 414 (2012).
- [9] M. S. Dresselhaus, G. Chen, M.-Y. Tang, R.-G. Yang, H. Lee, D.-Z. Wang, Z.-F. Ren, J. P. Fleurial, and P. Gogna, New directions for low-dimensional thermoelectric materials, *Adv. Mater.* **19**, 1043 (2007).
- [10] A. L. Hochbaum, R.-K. Chen, R. D. Delgado, W.-J. Liang, E. C. Garnett, M. Najarian, A. Makumdar, and P.-D. Yang, Enhanced thermoelectric performance of rough silicon nanowires, *Nature (London)* **451**, 163 (2008).
- [11] X.-K. Gu, Y.-J. Wei, X.-B. Yin, B.-W. Li, and R.-G. Yang, Phononic thermal properties of two-dimensional materials, *Rev. Mod. Phys.* **90**, 041002 (2018).
- [12] A. Kasaeian, A. T. Eshghi, and M. Sameti, A review on the applications of nanofluids in solar energy systems, *Renew. Sustain. Energy Rev.* **43**, 584 (2015).
- [13] F. Han, N. Andrejevic, and M.-D. Li, A hidden dimension to explore new thermoelectrics, *Joule* **2**, 16 (2018).
- [14] T. S. Li and G. L. Galli, Electronic properties of MOS<sub>2</sub> nanoparticles, *J. Phys. Chem. C* **111**, 16192 (2007).
- [15] G.-H. Gong, Y.-X. Zhang, W. Chen, J.-W. Chu, T.-Y. Lei, J.-R. Pu, L.-P. Dai, C.-Y. Wu, Y.-H. Cheng, T.-Y. Zhai, L. Li, and J. Xiong, Electronic and optoelectronic applications based on 2D novel anisotropic transition metal dichalcogenides, *Adv. Sci.* **4**, 1700231 (2017).
- [16] M. Khazaei, M. Arai, T. Sasaki, M. Estili, and Y. Sakka, Two-dimensional molybdenum carbides: Potential thermoelectric materials of the MXene family, *Phys. Chem. Chem. Phys.* **16**, 7841 (2014).
- [17] T.-V. Vu, C. V. Nguyen, H. V. Phuc, A. A. Lavrentyev, O. Y. Khyzhun, N. V. Hieu, M. M. Obeid, D. P. Rai, H. D. Tong, and N. N. Hieu, Theoretical prediction of electronic, transport, optical, and thermoelectric properties of Janus monolayers In<sub>2</sub>XO ( $X = S, Se, Te$ ), *Phys. Rev. B* **103**, 085422 (2021).
- [18] S. Demirci, N. Avazlı, E. Durgun, and S. Cahangirov, Structural and electronic properties of monolayer group III monochalcogenides, *Phys. Rev. B* **95**, 115409 (2017).
- [19] A. Shafique and Y. H. Shin, Thermoelectric and phonon transport properties of two-dimensional IV-VI compounds, *Sci. Rep.* **7**, 506 (2017).
- [20] W.-X. Lin, S.-D. Liang, C.-S. He, W.-C. Xie, H.-Y. He, W.-X. Mai, J.-S. Li, and D.-X. Yao, Stabilities and novel electronic structures of three carbon nitride bilayers, *Sci. Rep.* **9**, 1025 (2019).
- [21] Y. Dong, C. Zhang, M. Meng, M. M. Groves, and J. Lin, Novel two-dimensional diamond like carbon nitriles with extraordinary elasticity and thermal conductivity, *Carbon* **138**, 319 (2018).
- [22] A. Bafekry, M. Yagmurcukardes, B. Akgenc, M. Ghergherehchi, and B. Mortazavi, First-principles investigation of electronic, mechanical and thermoelectric properties of graphene-like XBi ( $X = Si, Ge, Sn$ ) monolayers, *Phys. Chem. Chem. Phys.* **23**, 12471 (2021).
- [23] S. B. Touski, Structural, electrical, and Rashba properties of monolayer Janus Si<sub>2</sub>XY ( $X, Y = P, As, Sb, \text{ and } Bi$ ), *Phys. Rev. B* **103**, 165404 (2021).
- [24] N. Niasadegh, M. Naseri, and S. Rezaee, Structural, electronic and optical properties of GeX ( $X = N, P, \text{ and } As$ ) monolayer: under stress and strain conditions, *Opt. Quant. Electron.* **53**, 502 (2021).
- [25] N. Ghobadi and S. B. Touski, Structural and electrical properties of bilayer SiX ( $X = N, P, As, \text{ and } Sb$ ), *J. Phys.: Condens. Matter.* **33**, 285502 (2021).
- [26] C. Barreteau, B. Michon, C. Besnard, and E. Giannini, High-pressure melt growth and transport properties of SiP, SiAs, GeP, and GeAs 2D layered semiconductors, *J. Cryst. Growth* **443**, 75 (2016).
- [27] W.-X. Lin, S.-D. Liang, J.-S. Li, and D.-X. Yao, Phonon dispersions and electronic structures of two-dimensional IV-V compounds, *Carbon* **172**, 345 (2021).
- [28] B. Özdamar, G. Özbal, M. N. Çinnar, K. Sevim, G. Kurt, B. Kaya, and H. Sevinçli, Structural, vibrational, and electronic properties of single-layer hexagonal crystals of group IV and V elements, *Phys. Rev. B* **98**, 121401(R) (2018).
- [29] H. Li, D.-C. Zhou, Q.-Y. He, N. Si, B.-W. Xin, S.-Y. Bu, Q.-M. Ji, H. Li, H. Fuchs, and T.-C. Niu, Experimental realization and phase engineering of a two-dimensional SnSb binary honeycomb lattice, *ACS Nano* **15**, 16335 (2021).
- [30] C. S. Jung, D. Kim, S. Cha, Y. Myung, F. Shojaei, F. Shojaei, H. G. Abbas, J. A. Lee, E. H. Cha, J. Park, and H. S. Kang, Two-dimensional GeAs with a visible range band gap, *J. Mater. Chem. A* **6**, 9089 (2018).
- [31] E. J. Skoug and D. T. Morelli, Role of Lone-Pair Electrons in Producing Minimum Thermal Conductivity in Nitrogen-Group Chalcogenide Compounds, *Phys. Rev. Lett.* **107**, 235901 (2011).
- [32] Y.-S. Zhang, E. Skoog, J. Cain, V. Ozolins, D. Morelli, and C. Wolverton, First-principles description of anomalously low lattice thermal conductivity in thermoelectric Cu-Sb-Se ternary semiconductors, *Phys. Rev. B* **85**, 054306 (2012).
- [33] S. N. Guin, A. Chatterjee, D. S. Negi, R. Datta, and K. Biswas, High thermoelectric performance in tellurium free p-type AgSbSe<sub>2</sub>, *Energy Environ. Sci.* **6**, 2603 (2012).
- [34] Z. Feng, T. Jia, J. Zhang, and Y.-S. Zhang, Dual effects of lone-pair electrons and rattling atoms in CuBiS<sub>2</sub> on its ultralow thermal conductivity, *Phys. Rev. B* **96**, 235205 (2017).
- [35] Z. Zhang, R. Zhang, N. Qi, Y. Wu, and Z. Chen, Microscopic origin of the extremely low thermal conductivity and outstanding thermoelectric performance of BiSbX<sub>3</sub> ( $X = S, Se$ ) revealed by first-principles study, *Phys. Chem. Chem. Phys.* **22**, 15559 (2020).
- [36] H.-M. Wang, G.-Z. Qin, Z.-Z. Qin, G.-J. Li, Q. Wang, and M. Hu, Lone-pair electrons do not necessarily lead to low lattice thermal conductivity: An exception of two-dimensional penta-CN<sub>2</sub>, *J. Phys. Chem. Lett.* **9**, 2474 (2018).
- [37] G. Kresse and J. Furthmüller, Efficiency of ab-initio total energy calculations for metals and semiconductors using a plane-wave basis set, *Comput. Mater. Sci.* **6**, 15 (1996)
- [38] G. Kresse and J. Hafner, *Ab initio* molecular dynamics for liquid metals, *Phys. Rev. B* **47**, 558(R) (1993).

- [39] J. P. Perdew, K. Burke, and M. Ernzerhof, Generalized Gradient Approximation Made Simple, *Phys. Rev. Lett.* **77**, 3865 (1996).
- [40] P. E. Blöchl, Projector augmented-wave method, *Phys. Rev. B* **50**, 17953 (1994).
- [41] H. J. Monkhorst and J. D. Pack, Special points for Brillouin-zone integrations, *Phys. Rev. B* **13**, 5188 (1976).
- [42] E. Sjöstedt, L. Nordström, and D. J. Singh, An alternative way of linearizing the augmented plane-wave method, *Solid State Commun.* **114**, 15 (2000).
- [43] D. J. Singh and L. Nordstrom, *Planewaves, Pseudopotentials, and the LAPW Method* (Springer, New York, 2006).
- [44] P. Blaha, K. Schwarz, G. Madsen, D. Kvasnicka, and J. Luitz, WIEN2k: An augmented plane wave + local orbitals program for calculating crystal properties (Karlheinz Schwarz, Technical University at Wien, Austria, 2001).
- [45] F. Tran and P. Blaha, Accurate Band Gaps of Semiconductors and Insulators with a Semilocal Exchange-Correlation Potential, *Phys. Rev. Lett.* **102**, 226401 (2009).
- [46] A. Togo and I. Tanaka, First principles phonon calculations in materials science, *Scr. Mater.* **108**, 1 (2015).
- [47] M. Omini and A. Sparavigna, An iterative approach to the phonon Boltzmann equation in the theory of thermal conductivity, *Phys. B (Amsterdam, Neth.)* **212**, 101 (1995).
- [48] M. Omini and A. Sparavigna, Beyond the isotropic-model approximation in the theory of thermal conductivity, *Phys. Rev. B* **53**, 9064 (1996).
- [49] W. Li, J. Carrete, N. A. Katcho, and N. Minggo, ShengBTE: A solver of the Boltzmann transport equation for phonons, *Comput. Phys. Commun.* **185**, 1747 (2014).
- [50] G. K. H. Madsen and D. J. Singh, BoltzTraP: A code for calculating band-structure dependent quantities, *Comput. Phys. Commun.* **175**, 67 (2006).
- [51] J.-S. Qiao, X.-H. Kong, Z.-X. Hu, F. Yang, and W. Ji, High-mobility transport anisotropy and linear dichroism in few-layer black phosphorus, *Nat. Commun.* **5**, 4475 (2014).
- [52] See Supplemental Material at <http://link.aps.org/supplemental/10.1103/PhysRevB.105.075431> for the structural parameters, the electronic band structures, the phononic spectra, and the lattice thermal conductivity in other  $\text{Ge}_2\text{Y}_2$  monolayers.
- [53] A. Savin, O. Jepsen, J. Flad, O. K. Andersen, and H. G. Vonschnering, Electron localization in solid-state structures of the elements: the diamond structure, *Angew. Chem., Int. Ed. Engl.* **31**, 187 (1992).
- [54] R. J. Gillespie and R. S. Q. Nyholm, Inorganic stereochemistry, *Quant. Rev., Chem. Soc.* **11**, 339 (1957).
- [55] Li. Wu and M. Natalio, Ultralow lattice thermal conductivity of the fully filled skutterudite  $\text{YbFe}_4\text{Sb}_{12}$  due to the flat avoided-crossing filler modes, *Phys. Rev. B* **91**, 144304 (2015).
- [56] A. S. Nissimagoudar, Z. Rashid, J. Ma, and W. Li, Lattice thermal transport in monolayer group 13 monochalcogenides MX ( $M = \text{Ga, In}$ ;  $X = \text{S, Se, Te}$ ): Interplay of atomic mass, harmonicity, and lone-pair-induced anharmonicity, *Inorg. Chem.* **59**, 14899 (2020).
- [57] H. H. Huang, X. F. Fan, D. J. Singh, and W. T. Zheng, The thermal and thermoelectric transport properties of SiSb, GeSb, and SnSb monolayers, *J. Mater. Chem. C* **7**, 10652 (2019).
- [58] W.-J. Qiu, L.-L. Xi, P. Wei, X.-Z. Ke, J.-H. Yang, and W.-Q. Zhang, Part-crystalline part-liquid state and rattling-like thermal damping in materials with chemical-bond hierarchy, *Proc. Natl. Acad. Sci. USA* **111**, 15031 (2014).
- [59] D.-F. Yang, W. Yao, Y.-C. Yan, W.-J. Qiu, L.-J. Guo, X. Lu, C. Uher, X.-D. Han, G.-Y. Wang, and T. Yang, Intrinsically low thermal conductivity from a quasi-one-dimensional crystal structure and enhanced electrical conductivity network via Pb doping in  $\text{SbCrSe}_3$ , *npj Asia Mater.* **9**, e387 (2017).
- [60] Y. Xiao, C. Chang, Y.-L. Pei, D. Wu, K.-L. Peng, X.-Y. Zhou, S.-K. Gong, J.-Q. He, Y.-S. Zhang, Z. Zeng, and L.-D. Zhao, Origin of low thermal conductivity in  $\text{SnSe}$ , *Phys. Rev. B* **94**, 125203 (2016).
- [61] E. J. Skoug, J. D. Cain, and D. T. Morelli, Structural effects on the lattice thermal conductivity of ternary antimony- and bismuth-containing chalcogenide semiconductors, *Appl. Phys. Lett.* **96**, 181905 (2010).
- [62] C.-G. Fu, T.-J. Zhu, Y.-Z. Pei, H.-H. Xie, H. Wang, G. J. Snyder, Y. Liu, Y.-T. Liu, and X.-B. Zhao, High band degeneracy contributes to high thermoelectric performance in p-type half-Heusler compounds, *Adv. Energy Mater.* **4**, 1400600 (2014).
- [63] Y. Tang, Z. Gibbs, L. Agapito, G.-D. Li, H. S. Kim, M. B. Nardelli, G. J. Snyder, and S. Curtarolo, Convergence of multi-valley bands as the electronic origin of high thermoelectric performance in  $\text{CoSb}_3$  skutterudites, *Nat. Mater.* **14**, 1223 (2015).
- [64] J.-Z. Xin, Y.-L. Tang, X.-B. Zhao, H.-G. Pan, and T.-J. Zhu, Valleytronics in thermoelectric materials, *npj Quant. Mater.* **3**, 2397 (2018).